Elsevier Editorial System(tm) for Ocean Engineering

Manuscript Draft

Manuscript Number: OE-D-17-01187R2

Title: 3D motion dynamics of axisymmetric bodies falling through water

Article Type: Full length article

Keywords: Dropped cylinder; Slamming; Slender body; 2D+t theory; Impulsively started flow; 3D motion

Corresponding Author: Dr. Hagbart S. Alsos, PhD

Corresponding Author's Institution: SINTEF Ocean

First Author: Hagbart S. Alsos, PhD

Order of Authors: Hagbart S. Alsos, PhD; Odd M Faltinsen, Professor, PhD

Abstract: A new simplified method for analysis of 3D motion dynamics of axisymmetric slender bodies falling from air through water is presented. Slender-body theory for potential flow of incompressible water is combined with 2D+t theory to account for viscous cross-flow separation in the submerged phase. The effect of flow separation from the upstream end of a pipe plays an important role. Furthermore, asymmetric vortex shedding triggering important 3D motions is considered. The water impact loads are based on strip theory and empirical slamming coefficients together with added mass and buoyancy loads. The theory is validated by comparing numerical analyses with experimental drop tests of pipes performed by Aanesland (1987). Error analyses of the theoretical method are performed and compared with tests to explore the sensitivity to input variations.

3D motion dynamics of axisymmetric bodies falling through water

Hagbart S. Alsos [a] *, Odd M. Faltinsen [b]

[a] SINTEF Ocean, Department of Ocean Engineering, Otto Nielsens veg 10, 7052 Trondheim, Norway

[b] NTNU, Department of Marine Technology, Otto Nielsens veg 10, 7052 Trondheim, Norway

* Corresponding author: Hagbart.Alsos@sintef.no

ABSTRACT

A new simplified method for analysis of 3D motion dynamics of axisymmetric slender bodies falling from air through water is presented. Slender-body theory for potential flow of incompressible water is combined with *2D+t* theory to account for viscous cross-flow separation in the submerged phase. The effect of flow separation from the upstream end of a pipe plays an important role. Furthermore, asymmetric vortex shedding triggering important 3D motions is considered. The water impact loads are based on strip theory and empirical slamming coefficients together with added mass and buoyancy loads. The theory is validated by comparing numerical analyses with experimental drop tests of pipes performed by Aanesland (1987). Error analyses of the theoretical method are performed and compared with tests to explore the sensitivity to input variations.

Keywords: Dropped cylinder, Slamming, Slender body, 2D+t theory, Impulsively started flow, 3D motion

1 Introduction

Failure of offshore crane operations leading to objects being dropped to sea represents a major hazard for subsea structures, pipelines and risers, and is therefore given attention in offshore engineering. Safety engineering on the Norwegian shelf is typically performed using guidelines and recommended practices such as DNVGL(2017b) and DNVGL(2017a). These present simplified and analytical approaches to define dropped object rates, impact damage and hit probability. As a result, they tend to

be very conservative as the most unfavourable drop conditions are considered. More accuracy with respect to hit location and impact energy could be achieved by adopting more detailed methods such as Computational Fluid Dynamics (CFD). However, since the problem requires a large set of analyses to cover all types of lifted objects and their statistical variations, detailed analysis by CFD becomes computationally demanding and impractical. Simplified rational approaches validated against model tests are therefore required. This is performed in the following. The focus is placed on tube shaped objects dropped to sea, e.g. drill collars, tubing, casings, and scaffolding. An axisymmetric rigid slender body falling through water with initial conditions from water impact is considered. A 3D solver considering the nonlinear behavior of slender bodies is established and compared with tests by Aanesland (1987).

The responses of dropped object in water have been performed by several authors. Aanesland (1987), and Aanesland and Huse (1986), were among the first to illustrate the various drop patterns of cylindrical objects through experiments and numerical analyses. The description of drop patterns was later adopted by DNVGL's recommended practice on the topic, DNVGL(2017b). Other authors have studied the matter for applications such as deployment of cylindrical mines. For instance, Chu et al. (2005) have presented experimental results of falling objects by dropping three cylinders of various lengths into a pool. The controlled parameters are length-to-diameter ratio, center of mass location, initial velocity and drop angle. Six trajectory patterns (straight, spiral, flip, flat, seesaw, combination) were detected. The center of mass position had the largest influence on the trajectory. Mann et al. (2007) made numerical studies of the fall of a cylindrical mine and referred to model tests by Valent and Holland (2001). Mann et al. (2007) categorized the trajectories as presented in Table 1.

Table 1: Trajectory description of submerged dropped cylinders, as described by Mann et al (2007)

Drop behavior	Description
Straight motion	Occurs when the cylinder maintains a horizontal or vertical orientation. A necessary condition is that centers of mass and buoyancy coincide.
Straight-slant motion	A pattern for which the body shows a slant movement during a straight fall and is a consequence of directional instability.
Nose-turn motion	Involves the quick change of the orientation of the body and is associated with directional instability. This motion occurs typically when the body drops with an oblique angle or mass center is slightly ahead of the buoyancy center.
Seesaw motion	Pitch oscillations that occur when the mass and buoyancy centers are close.
Tumbling motion	The cylinder flips over itself.
Travel motion	A stable motion with significant horizontal movement but no significant pitch or yaw oscillations. In the experiments, this pattern was observed mostly at oblique drops and the mass centers are somewhat far from the buoyancy center.
Spiral motion	A 3D motion that can occur when a cylinder falls through water and a straight or seesaw motion develops into spinning motion due to dynamic instability.
Combined motion	A combination of the motions described above. These may follow in sequence or as combined trajectories.

Similar observations have also been performed by Chu et al (2005); also here for mine shaped cylinders. The L/D ratios presented in these studies were typically in the order of 3 to 6. Aanesland (1987) described drop trajectories for dropped drill pipes with intact end caps having L/D ratios in the order of 40. This was documented through model tests and numerical analyses based on planar slender body theory with viscous corrections. Both submerged and above free surface drop scenarios were addressed. Through his work, he detected another and dominant trajectory pattern for slender bodies, which we call the "*falling-leaf motion*". This is illustrated in Figure 1(a) from a simulation in 3D of a 14 m long drill pipe with end caps, diameter 0.346 m, and weight of 1400 kg, which is dropped to sea. The applied drop height is 30 m and the initial drop angle towards the calm free surface is 60 degrees. Both the water entry and submerged phases are considered. During the submerged phase, the pipe typically exhibits a trajectory as shown in Figure 1, consisting of two paths AB and BC. Along path

AB, the pipe receives an inflow with an angle α to the longitudinal axis which generates resistance and a de-stabilizing lift effect, see Figure 1(b). Another important resistance component is the pipe's weight in water when the nose points upwards. Maximum excursion is reached at point B. After point B, the pipe starts to "fall" towards the sea floor, exhibiting an oscillatory horizontal motion like a "falling leaf in air".

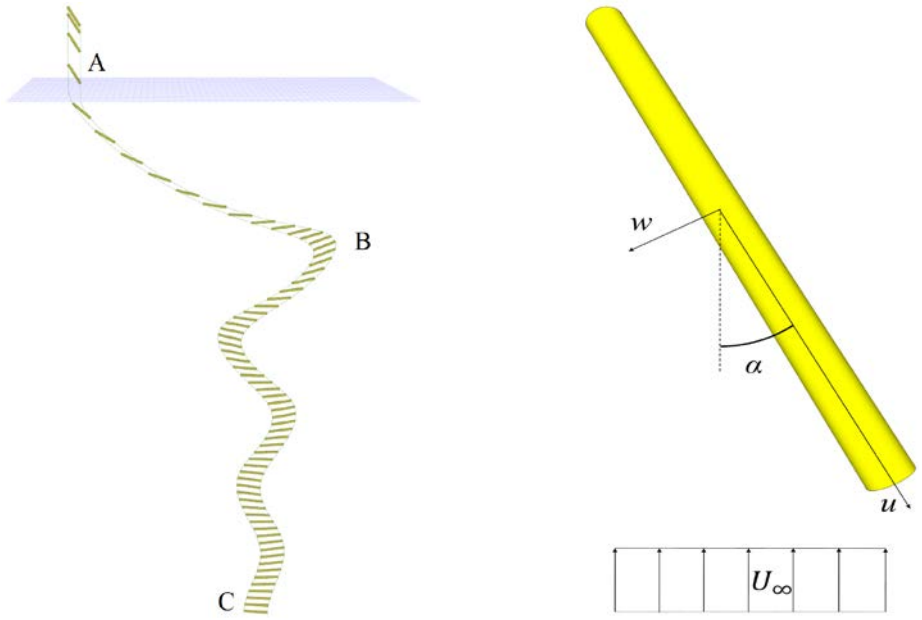

(a) (b)

Figure 1: (a) Characteristic drop trajectory. The falling-leaf motion is illustrated from B to C. (b) Incidental flow U_∞ at an angle α to the longitudinal axis.

In the following we present the theory for 3D response of falling submerged pipes with end caps. This differs from Aanesland (1987), who studied planar motions of a free-falling rigid pipe with end caps. Aanesland (1987) assumed that the centers of gravity and buoyancy coincided while we allow them to differ. Aanesland (1987) further applied slender-body theory for potential flow with a correction factor adopted from ship maneuvering to express lifting effects. The cross-flow principle and empirical drag coefficients were used to express the transverse viscous load. This procedure does not account for that cross-flow separation differs along the body, as known from yawed missile analysis Zdravkovich (2003) and CFD analysis of ship maneuver at forward speed, Durante et al, (2010). Our proposed

2D+t method accounts for varying cross-flow separation along a pipe and is combined with slender-body theory for potential flow. We also introduce transverse effects from asymmetric separation, as presented by Sarpkaya (2010).

2 Submerged behavior of dropped cylinder - theory

2.1 Governing equations in fully-submerged condition

We use sections 10.9.1 and 10.10.2 in Faltinsen (2005) to formulate the equations of motions of a fully submerged axisymmetric body. We introduce then a body-fixed coordinate system with definitions in Figure 2. The body-fixed coordinate system (x, y, z) has origin in the centre of gravity (COG) with the $x-$ axis along the symmetry axis of the body. The centre of buoyancy is at $(x_B, 0, 0)$. The velocity vector $\boldsymbol{V}$ of the COG has components (u, v, w) and the angular velocity vector $\boldsymbol{\Omega}$ of the body has components (p, q, r) in the body-fixed coordinate system. The Euler angles yaw (ψ), pitch (Θ) and roll (Φ) of the body are introduced. The order is yaw, pitch and roll.

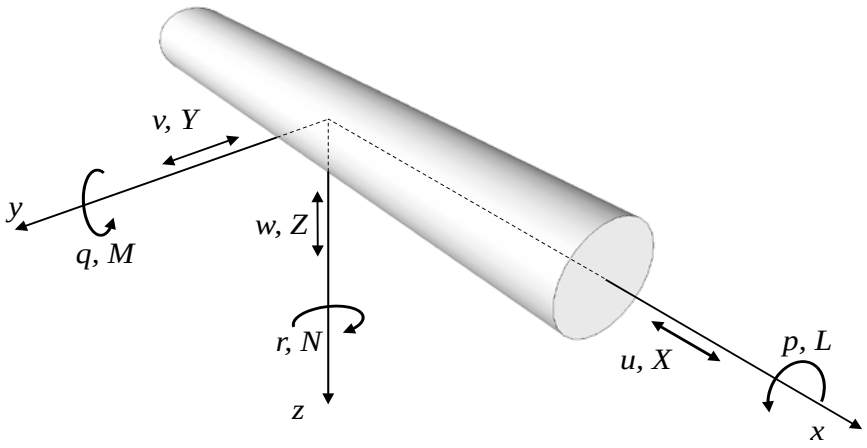

Figure 2: Body-fixed coordinate system (x, y, z) *with origin in the centre of gravity* (COG) *of an axisymmetric body. The COG has velocity* $\boldsymbol{v} = (u, v, w)$ *and the angular velocity of the body is* $\boldsymbol{\Omega} = (p, q, r)$. *The external forces and moments with respect to* COG *acting on the body are respectively* (X, Y, Z) *and* (L, M, N).

It follows from Newton's second law that

$$\begin{aligned} M[\dot{u} + qw - rv] &= X - Mg\sin\Theta \\ M[\dot{v} + ru - pw] &= Y + Mg\cos\Theta\sin\Phi \\ M[\dot{w} + pv - qu] &= Z + Mg\cos\Theta\cos\Phi \end{aligned} \tag{1}$$

Here M is the mass of the body, g is acceleration of gravity and $(\mathrm{X}, \mathrm{Y}, \mathrm{Z})$ are the hydrodynamic and hydrostatic forces acting on the body. We need also to consider external moments about the *x*, *y* and *z*-axis. We can then write

$$\begin{aligned} I_{44}\dot{p} - (I_{55} - I_{66})qr - I_{64}(\dot{r} + pq) &= L \\ I_{55}\dot{q} - (I_{66} - I_{44})rp - I_{64}(r^2 - p^2) &= M \\ I_{66}\dot{r} - (I_{44} - I_{55})pq - I_{64}(\dot{p} - qr) &= N \end{aligned} \tag{2}$$

Here I_{jj} is the mass moment of inertia of the j^{th} mode and I_{jk} is the product of mass inertia with respect to the coordinate system(x, y, z). Furthermore, *L*, *M* and *N* are the external moments about the *x*-, *y*- and *z*-axis, respectively. Note that *M* has been used as a symbol for both mass and an external moment component. We can set $I_{55} = I_{66}$, $I_{64} = 0$ for the considered axisymmetric body. Since the considered hydrodynamic loads are pressure loads, the moment component *L* is zero, which means that nonzero *p* can only be a consequence of initial conditions.

The translational motions of the body are referenced to an Earth-fixed coordinate system (X_E, Y_E, Z_E). According to equation (10.113) and (10.114) in Faltinsen (2005) we can write

$$\begin{aligned} \frac{dX_E}{dt} &= u\cos\Theta\cos\Psi + v(\sin\Phi\sin\Theta\cos\Psi - \cos\Phi\sin\Psi) + w(\cos\Phi\sin\Theta\cos\Psi + \sin\Phi\sin\Psi) \\ \frac{dY_E}{dt} &= u\cos\Theta\sin\Psi + v(\sin\Phi\sin\Theta\sin\Psi + \cos\Phi\cos\Psi) + w(\cos\Phi\sin\Theta\sin\Psi - \sin\Phi\cos\Psi) \\ \frac{dZ_E}{dt} &= -u\sin\Theta + v\sin\Phi\cos\Theta + w\cos\Phi\cos\Theta \end{aligned} \tag{3}$$

and

$$\frac{d\Theta}{dt} = q\cos\Phi - r\sin\Phi$$
$$\frac{d\Phi}{dt} = p + q\sin\Phi\tan\Theta + r\cos\Phi\tan\Theta$$
$$\frac{d\Psi}{dt} = (q\sin\Phi + r\cos\Phi)\sec\Theta \quad (4)$$

We then have presented 12 nonlinear differential equations given by equations (1), (2), (3) and (4) with the 12 unknowns $u, v, w, p, q, r, X_E, Y_E, Z_E, \Theta, \Phi$ and Ψ. To solve these equations numerically we need to express the external forces and moments acting on the body and specify initial conditions.

The external forces and moments will be associated with hydrostatics, added mass acceleration loads based on potential flow as well as velocity-dependent hydrodynamic loads with lift effects based on potential flow and viscous loads. We will use superscripts *hs*, *am*, *pot* and *visc* to identify them. In addition, we use the superscript *L* to identify lift forces and moments associated with asymmetric vortex shedding.

2.2 Hydrostatics

We get the following hydrostatic force and moment components for the considered submerged axisymmetric body

$$X^{hs} = \rho\nabla g\sin\Theta$$
$$Y^{hs} = -\rho\nabla g\cos\Theta\sin\Phi$$
$$Z^{hs} = -\rho\nabla g\cos\Theta\cos\Phi$$
$$L^{hs} = 0 \quad (5)$$
$$M^{hs} = x_B\rho\nabla g\cos\Theta\cos\Phi$$
$$N^{hs} = -x_B\rho\nabla g\cos\Theta\sin\Phi$$

Here ∇ is the displaced volume of water by the body and ρ is the mass density of water.

2.3 Potential-flow added mass acceleration loads on a body in infinite fluid

We introduce the added mass coefficients A_{jk} according to potential flow in infinite and incompressible water Faltinsen (2005). Some of the coefficients are zero due to geometrical symmetry about the *x*-*z* and *x*-*y* plane. Furthermore, roll cannot induce any potential flow and since there are no viscous stresses in potential flow and the hydrodynamic pressure do not cause roll moments, the added mass roll moments are zero. This gives that only

$A_{11}, A_{22}, A_{26} = A_{62}, A_{33}, A_{35} = A_{53}, A_{55}, A_{66}$ are, in general, non-zero. Kochin et al (1964) have derived the nonlinear, non-lifting and non-viscous force and moment components in a body-fixed coordinate system on a maneuvering body in infinite fluid, see also Faltinsen (2005). The acceleration dependent force and moment components on the axisymmetric body can be expressed as

$$
\begin{aligned}
X^{am} &= -A_{11}\dot{u} \\
Y^{am} &= -(A_{22}\dot{v} + A_{26}\dot{r}) \\
Z^{am} &= -(A_{33}\dot{w} + A_{35}\dot{q}) \\
L^{am} &= 0 \\
M^{am} &= -(A_{53}\dot{w} + A_{55}\dot{q}) \\
N^{am} &= -(A_{62}\dot{v} + A_{66}\dot{r})
\end{aligned}
\tag{6}
$$

When cross-flow separation occurs, 2D U-tube experiments of a circular cylinder of diameter *D* in ambient harmonic oscillatory flow velocity amplitude U_m and period *T* show that cross-flow separation significantly affects the added mass coefficients for Keulegan-Carpenter number $KC = U_m T/D$ larger than about five, Sarpkaya (2010). The latter fact is not accounted for and is in general less important in our case due to the presence of the longitudinal motion. The importance of neglecting the influence of viscosity on the acceleration dependent hydrodynamic loads will be discussed in the analysis of the free-fall motion of a pipe. Some of the nonlinear potential flow terms by Kochin et al (1964) are parts of the slender-body theory expressions presented in the next section. There are in addition resistance terms in Kochin et al's expressions, which may matter in ship maneuvering analysis. However, significant empirical corrections due to viscous effects may be needed during the turning maneuver of a ship.

2.4 Potential-flow hydrodynamic forces and moments in steady flow

We use slender-body theory based on potential flow of incompressible water (Faltinsen, 2005) and assume no internal flow, which means that a pipe must be equipped with end caps. The velocity-dependent two-dimensional force components in the y- and z- directions can be expressed as

$$f_y^{2D} = u\frac{\partial}{\partial x}[a_{22}(v + xr)] \text{ and } f_z^{2D} = u\frac{\partial}{\partial x}[a_{33}(w - xq)] \tag{7}$$

where the two-dimensional added mass coefficients a_{22} and a_{33} are $\rho\pi D^2/4$ with D as the cross-sectional diameter. It is essential that the upstream condition at the body end is zero added mass, which implies an abrupt change in added mass at the upstream end of a pipe. If the downstream end is not pointed and no flow separation occurs before the downstream end, the flow is assumed to separate from the downstream end in the downstream direction. The consequence is a lift force. The following total force components follow

$$\begin{aligned} X^{pot} &= 0 \\ Y^{pot} &= \begin{cases} -a_{22sep}u\big(v + rx_{sep}\big), & u > 0 \\ a_{22sep}u\big(v + rx_{sep}\big), & u < 0 \end{cases} \\ Z^{pot} &= \begin{cases} -a_{33sep}u\big(w - qx_{sep}\big), & u > 0 \\ a_{33sep}u\big(w - qx_{sep}\big), & u < 0 \end{cases} \end{aligned} \tag{8}$$

Here x_{sep} is the *x*-coordinate where flow separation starts and $a_{jj\,sep}$ denotes a_{jj} at x_{sep}. The moment components are

$$\begin{aligned} L^{pot} &= 0 \\ M^{pot} &= \begin{cases} a_{33sep}ux_{sep}\big(w - qx_{sep}\big) + u\int_{x_{sep}}^{x_N} a_{33}(x)\,(w - xq)dx, & u > 0 \\ -a_{33sep}ux_{sep}\big(w - qx_{sep}\big) + u\int_{x_T}^{x_{sep}} a_{33}(x)\,(w - xq)dx, & u < 0 \end{cases} \\ N^{pot} &= \begin{cases} -a_{22sep}ux_{sep}\big(v + rx_{sep}\big) - u\int_{x_{sep}}^{x_N} a_{22}(x)\,(v + xr)dx, & u > 0 \\ a_{22sep}ux_{sep}\big(v + rx_{sep}\big) - u\int_{x_T}^{x_{sep}} a_{22}(x)\,(v + xr)dx, & u < 0 \end{cases} \end{aligned} \tag{9}$$

If we consider a pipe, flow separation starts at the upstream end and $a_{jj\,sep} = \rho\pi D^2/4$. The expressions show that the center of pressure is at x_N when $u > 0$ and at x_T when $u < 0$. Aanesland (1987) adopted an approach from ship maneuvering and set x_{sep}, except in the integral part, to be between 30% and 0% of the pipe length from the downstream end. x_{sep} is set at the downstream end in the evaluation of the integrals, which then represent destabilizing Munk moments for a non-lifting body. The argument in selecting x_{sep} in ship maneuvering analysis is diminishing cross-sectional areas in the aft body and associated flow separation. Furthermore, the drift angle in ship maneuvering is, in general, smaller than for a falling pipe in water.

2.5 Viscous velocity-dependent forces and moments

The longitudinal viscous force can be expressed in terms of frictional and drag coefficients. If we consider a pipe with length *L* and diameter *D* and there is turbulent axisymmetric flow along a smooth surface, we can write

$$X^{visc} = -0.5\rho C_F \pi D L u|u| - \frac{\rho}{8}\pi C_{Dx} D^2 u|u| \tag{10}$$

where the frictional coefficient

$$C_F = 0.0015 + \left(0.30 + 0.015\left(\frac{2L}{D}\right)^{0.4}\right) Rn^{-1/3} \tag{11}$$

is based on White (1972). Here $Rn = |u|L/\upsilon$ means the Reynolds number with υ as the kinematic viscosity coefficient. The assumptions are $10^6 < Rn < 10^9$ for purely longitudinal motion. Furthermore, C_{Dx} represents the sum of a fore body and base drag coefficient. The fore-body pressure drag coefficient for a pipe is 0.65 according to Hoerner (1958). Aanesland (1987) assumes laminar boundary layer flow when comparing with his model tests and applies the formula of Blasius, as described by Schlichting (1979), which states that $C_F = 1.328/\sqrt{Rn}$. In our formulation of frictional drag, we combine expressions for both laminar and turbulent boundary layer flow. For simplicity, we neglect the transition zone and assume turbulent flow for $Rn > 10^6$.

We express the drag-induced transverse force components, and pitch and yaw-moments due to flow separation as

$$
\begin{aligned}
Y^{visc} &= -\frac{\rho}{2}\int_{x_T}^{x_N} dx\; C_D(x)D(x)(v+xr)\sqrt{(v+xr)^2+(w-xq)^2} \\
Z^{visc} &= -\frac{\rho}{2}\int_{x_T}^{x_N} dx\; C_D(x)D(x)(w-xq)\sqrt{(v+xr)^2+(w-xq)^2} \\
M^{visc} &= \frac{\rho}{2}\int_{x_T}^{x_N} dx\; C_D(x)D(x)\,x(w-xq)\sqrt{(v+xr)^2+(w-xq)^2} \\
N^{visc} &= -\frac{\rho}{2}\int_{x_T}^{x_N} dx\; C_D(x)D(x)\,x(v+xr)\sqrt{(v+xr)^2+(w-xq)^2}
\end{aligned}
\tag{12}
$$

Here $D(x)$ is the cross-sectional diameter and $C_D(x)$ is the drag coefficient. By "drag-induced" we mean that we consider sectional forces along the local inflow velocity direction. The cross-flow principle leads to a strip theory approach and implies that the drag coefficient C_D is the same as assuming no hydrodynamic interaction between the strips, with an inflow velocity with components $(v+xr)$ and $(w-xq)$ along the *y* and *z* axis, respectively.

Extensive relevant research has been carried out for missiles with high angle of incidence between free stream velocity and missile longitudinal axis (Zdravkovich, 2003). The cross-flow separation starts at a distance from the pointed streamlined (ogive) nose similarly as shown in Figure 3. Werle (1979) carried out detailed flow visualization at different cross-sections. The results indicated that asymmetric cross-flow separation happens when $X > X_{as} = 4.2D/|\alpha|$ where the longitudinal coordinate from the nose is X. D is the constant diameter after the ogive nose and α is the angle between the incident flow and the missile longitudinal axis, as illustrated in Figure 1(b). The consequence of asymmetric cross-flow separation is a lateral force. Lamont and Hunt (1976) evaluated the normal drag and lateral force along a missile with an ogive nose based on pressure measurements. There is implicitly hydrodynamic interaction between the cross-sections causing largest C_D in the downstream part of a slender

axisymmetric body. We see indirectly an example on this in Figure 4 by a *2D+t* illustration of a pipe with a streamlined pointed nose. The transverse velocity of the body is assumed constant along the body after an initial time. The shed vorticity in Figure 4 is largest in the downstream part.

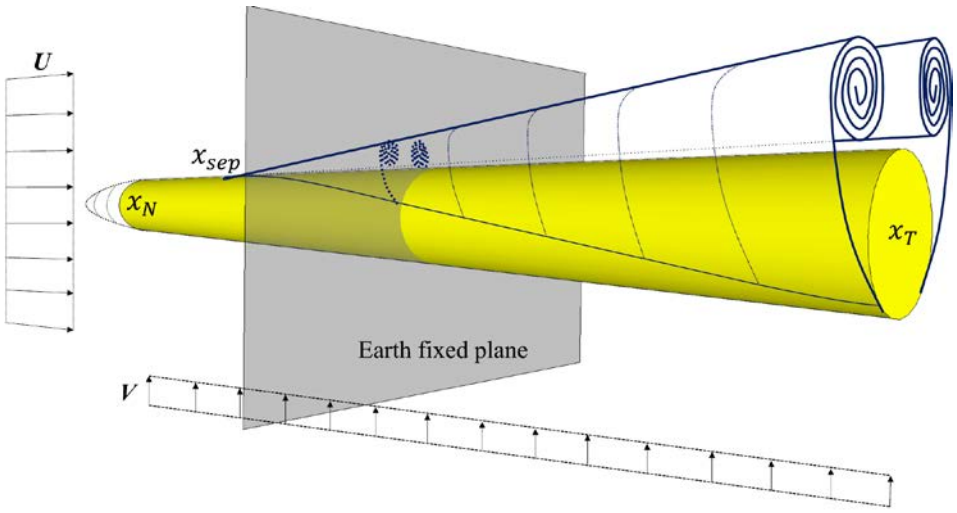

Figure 3: 2D+t analysis of a cylinder with constant forward velocity U and constant transverse velocity V. The cross-flow starts to separate at longitudinal distance x_{sep} from the front end.

In addition to drag, a lift-induced force and moment components associated with asymmetric vortex shedding is introduced. This can be written as follows, where $C_L(x)$ is an *x*-dependent lift coefficient.

$$
\begin{aligned}
Y^L &= \frac{\rho}{2}\int_{x_T}^{x_N} dx\, C_L(x)D(x)(w-xq)\sqrt{(v+xr)^2+(w-xq)^2} \\
Z^L &= -\frac{\rho}{2}\int_{x_T}^{x_N} dx\, C_L(x)D(x)(v+xr)\sqrt{(v+xr)^2+(w-xq)^2} \\
M^L &= \frac{\rho}{2}\int_{x_T}^{x_N} dx\, C_L(x)D(x)\,x(v+xr)\sqrt{(v+xr)^2+(w-xq)^2} \\
N^L &= \frac{\rho}{2}\int_{x_T}^{x_N} dx\, C_L(x)D(x)\,x(w-xq)\sqrt{(v+xr)^2+(w-xq)^2}
\end{aligned}
\tag{13}
$$

We will generalize the *2D+t* analysis as presented in Faltinsen (2005). The problem is analyzed in the time domain in different Earth-fixed cross planes as illustrated in Figure 3. It is the flow development in impulsively started flow in an Earth-fixed cross plane that determines the drag coefficient. This depends on how much the cylinder has moved in this Earth-fixed cross plane relative to its radius. We

will use experiments by Sarpkaya (1966, 2010) for laminar boundary layer conditions and suggest how to scale the results to other Reynolds number conditions. The experimental results are based on constant unidirectional transverse cylinder motions after a nearly impulsive start. We modify the results by accounting for the fact that the cylinder motions are spatially varying and are not unidirectional. It is assumed implicitly that the transverse force per unit length is in the direction of the cross-sectional velocity of the pipe.

We start out by considering a given time, t, and want to find how the drag coefficient $C_D(x)$ varies along the pipe at a certain time frame. The result will depend on previous values of angular velocities as well as longitudinal velocities. We must account for the possibility that u can be both positive and negative and that the sign changes as during a falling leaf motion. We define an initial time t_0, which is the time instant when u starts to be either positive or negative. We consider a given position x at time t, which must be considered for all values of *x*. There are two scenarios when $u > 0$. One scenario is that the time t_{0x} when the nose first penetrated the Earth-fixed plane located at x at time t is larger or equal to the time t_0. We will exemplify the procedure by setting previous values of angular velocities as well as longitudinal velocities to be constant. We can write

$$x_N - x = \int_{t_{0x}}^{t} u dt = u(t - t_{0x}) \tag{14}$$

when $t_{0x} < t_0$, the initial *x*-coordinate x_0 of the Earth-fixed plane located at x at time t is given by

$$x_0 - x = \int_{t_0}^{t} u dt = u(t - t_0) \tag{15}$$

We have to identify the *x*-coordinate x_p of the Earth-fixed plane at any time instant $\max(t_{0x}, t_0) < \tau < t$. It is given by either

$$x_N - x_P = u(\tau - t_{0x}) \text{ or } x_0 - x_P = u(\tau - t_0) \tag{16}$$

We can express how much the cylinder has moved transversely at *x* in the *y*-and *z*-directions as well as totally since the cylinder penetrated the considered Earth-fixed plane at its nose or at initial time as

$$s_y = \int_{t_{0x}}^{t} [v(\tau) + x_P(\tau) r(\tau)]\, d\tau = v\frac{x_N - x}{u} + \frac{r}{u}[x_N(x_N - x) - \frac{1}{2}(x_N - x)^2]$$
$$s_z = \int_{t_{0x}}^{t} [w(\tau) - x_P(\tau) q(\tau)]\, d\tau = w\frac{x_N - x}{u} - \frac{q}{u}[x_N(x_N - x) + \frac{1}{2}(x_N - x)^2] \quad (17)$$
$$s = \sqrt{s_y^2 + s_z^2}$$

If $t_{0x} < t_0$, we replace x_N by x_0 in the expressions for *s*.

We start by considering a body with streamlined upstream end and introduce the non-dimensional variable

$$t' = \frac{s}{R} - 0.351 \quad (18)$$

as a generalization of Faltinsen (2005). Here $R(x)$ is the cross-sectional radius. If $t' < 0$, flow separation has not occurred and $C_D = 0$. If $t' > 0$, we base the drag coefficient on experimental results by Sarpkaya (1966) and write by curve-fitting for $t' < 25$ that

$$C_D = \left(p_1 t'^5 + p_2 t'^4 + p_3 t'^3 + p_4 t'^2 + p_5 t' + p_6\right)\frac{C_{D\infty}}{1.2} \quad (19)$$

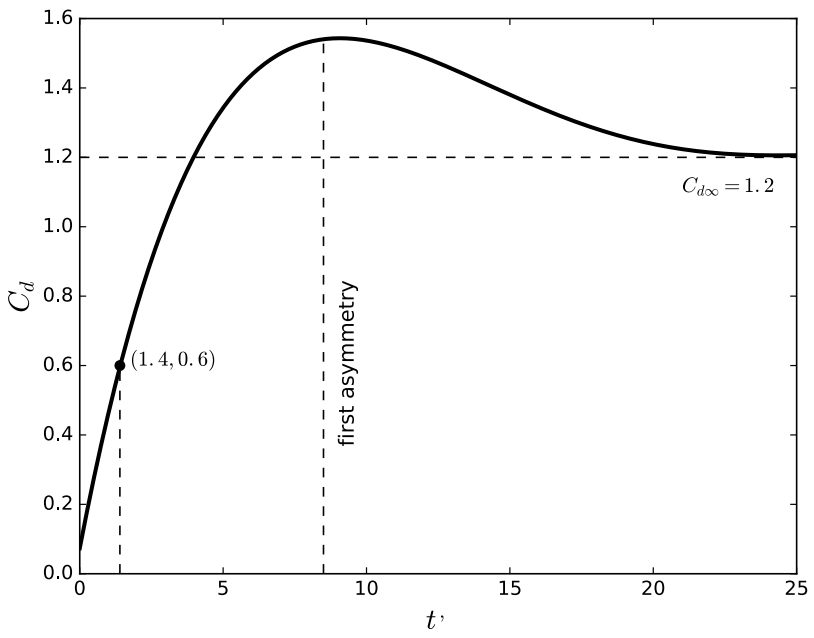

Figure 4: Drag coefficient C_D^{lam} for a circular cylinder with nearly impulsively started laminar boundary layer flow versus non-dimensional time t'. Approximation of experiments by Sarpkaya (1966).

Here the non-dimensional p_i-coefficients are given for the range $0 < t' < 25$ in Table 2. When $t' > 25$, then $C_D = C_{D\infty}$, i.e. the drag coefficient in steady-state conditions with steady ambient flow.

Table 2: Polynomial p_i-coefficients for eq. (19) as visualized in Figure 4 in the range $0 < t' < 25$.

p_1	p_2	p_3	p_4	p_5	p_6
$2.4805 \cdot 10^{-7}$	$-3.647 \cdot 10^{-5}$	$1.9058 \cdot 10^{-3}$	$-4.4173 \cdot 10^{-2}$	$4.3146 \cdot 10^{-1}$	$7.3386 \cdot 10^{-2}$

The term $C_{D\infty}$ is equal to 1.2 in the experiments by Sarpkaya (1966) corresponding to laminar boundary layer flow. The results are presented in Figure 4. We can follow a similar procedure when $u < 0$. We let the time t_{0x} mean the time when the tail first penetrated the Earth-fixed plane located at x at time t, which should be larger or equal to the time t_0. We can then find t_{0x} by

$$x_T - x = \int_{t_{0x}}^{t} u dt \tag{20}$$

When $t_{0x} < t_0$, then the initial x-coordinate x_0 of the considered Earth-fixed plane is given by

$$x_0 - x = \int_{t_0}^{t} u dt \tag{21}$$

We must identify the x-coordinate x_P of the considered Earth-fixed plane at any time instant $\max(t_{0x}, t_0) < \tau < t$. We have either

$$x_T - x_P = \int_{t_{0x}}^{t} u dt \tag{22}$$

or

$$x_0 - x_P = \int_{t_0}^{t} u dt \tag{23}$$

We can then proceed as we did for $u > 0$.

Classical experimental results for 2D circular cylinder can be used to determine the Reynolds number dependence of $C_{D\infty}$. Possible surface roughness effects as well as turbulence in the incident flow can be considered. There will be 3D flow effects at the downstream end of the cylinder that cannot be evaluated by a *2D+t* theory. A pragmatic way is to let the *2D+t* sectional loads go linearly to zero at the downstream end over the order of the diameter. The suggested procedure is quasi-steady, which means that it may not be consistent with known experimental results as a function of the Keulegan-Carpenter number. Furthermore, transition between laminar and turbulent boundary layer flow cannot be accounted for. Ersdal and Faltinsen (2006) studied the latter effect experimentally for a yawed cylinder at forward speed. If we define an incident flow velocity U_∞ with angle α relative to the cylinder axis, then the Reynolds number $U_\infty D \sin\alpha/\nu$ can be used to define critical flow regimes in

the same way as the Reynolds number for 2D cross-flow past a circular cylinder. Since the flow will separate from the upstream end of a pipe, the described *2D+t* approach must be modified such as there is a non-zero drag coefficient at the upstream end. We will as an example set the drag coefficient C_{DU} at the upstream end equal to half its steady value $C_{D\infty}$ to reflect roughly the three-dimensionality of the flow at the nose. As illustrated in Figure 4, this is obtained by expressing t' as follows:

$$t' = s/R + 1.4 \tag{24}$$

We will later investigate the sensitivity of the choice of the drag coefficient at the upstream end by comparing with model tests of free-fall motion of a pipe in water.

The lift coefficient associated with eq. (13) can be approximated based on tests performed by Sarpkaya (2010) for an impulsively started flow. We use the following approximation

$$C_L = \begin{cases} K\, C_{La} \sin[\pi St(t' - 8)], & t' > 8 \\ 0, & \text{otherwise} \end{cases} \tag{25}$$

Here $St = f_v D/V$ is the Reynolds-number dependent Strouhal number with f_v as the vortex shedding frequency and V as the cross-flow ambient velocity. $St = 0.2$ is an approximate value in the experiments by Sarpkaya (2010). Furthermore, $K = \pm 1$ reflects that the sign of the initial lift at $t' = 8$ is stochastic. An example on lift coefficient amplitude C_{La} is 0.2 Sarpkaya (2010). However, higher values are possible. If we consider a pipe of constant diameter D and an angle α between a steady incident flow and the cylinder axis, the *2D+t* approach together with Sarpkaya's (1966) experiments show that asymmetric cross-flow separation with resulting side force happens when $X > X_{as} = 4.2D/|\tan\alpha|$, where X is the longitudinal coordinate from the nose. When $\alpha \to \pi/2$, $X_{as} \to \infty$. The result agrees reasonably with Werle (1979) for $|\alpha| \lesssim \pi/9$.

3 Validation and error analysis

We start by validating the effect of *2D+t* theory and choice of upstream drag coefficient as defined eq. (19) and eq. (24). This implies that we set the drag coefficient C_{DU} at the upstream end equal to half its steady value $C_{D\infty}$. This is then compared with model tests in air performed by Reif and Powell (1917) of transverse force Y on a fixed pipe of length *L* in a steady inflow velocity U_∞ with angle α relative to the cylinder axis, see Figure 1(b). Their model test conditions are *L/D* = 80 and Reynolds number $U_\infty D/\nu = 7.7 \cdot 10^3$. If we use the cross-flow principle for the viscous loads as, for instance, Aanesland (1987) does, it means by adding the potential flow lift force that the normalized force can be written as follows

$$\frac{Y}{0.5\rho U_\infty^2 LD} = \frac{\pi}{2}\frac{D}{L}\sin\alpha\cos\alpha + C_D \sin^2\alpha \tag{26}$$

Here ρ is the fluid density and C_D is the Reynolds-number dependent drag coefficient for 2D flow past a circular cylinder. From eq. (26) we see that the importance of the potential flow lift force decreases with decreasing *D/L*. It is further observed that the contribution from potential flow is equally important as the viscous part when $\alpha = 1°$ if we for the relevant Reynholds number set $C_D = 1.1$, *i*.e. $\alpha = \arctan(\frac{0.5\pi D}{LC_D})$.

A convenient way to investigate the variations in transverse force for various inflow angles is by investigating the force ratio $Y(\alpha)/[Y(\pi/2)\sin^2\alpha]$. For the smooth cylinder, Reif and Powell (1917) reported results for angles $\alpha = 10°, 20°, 30°, 40°,\ 50°, 60°, 70°$ and $80°$ with corresponding values 1.22, 1.15, 1.14, 1.07, 1.06, 1.03 and 1.01, respectively. If we use eq. (26) and apply the cross-flow principle for viscous drag, we get that $Y(\alpha)/[Y(\pi/2)\sin^2\alpha]$ is 1.10, 1.05, 1.03, 1.02 for $\alpha = 10°, 20°, 30°$and $40°$, respectively. When applying the *2D+t* theory for the viscous loads, we let the flow separate at the nose section with an upstream drag coefficient C_{DU} of half its steady value $C_{D\infty}$. The result is that Y(α) / $[Y(\pi/2)\sin^2\alpha]$ is 1.18, 1.09, 1.06 and 1.03 for $\alpha = 10°, 20°, 30°$and $40°$, respectively. We could have chosen a higher value of C_{DU} to get even better agreement with the

experimental results. However, experiments have also errors, which we do not know in the present case. We will rather leave C_{DU} as a parameter that we can vary when later comparing with experimental results for the free fall of a pipe through water.

In the following we will compare the theory from section 2 by use of numerical analysis towards drop tests performed by Aanesland (1987). Two set of model tests were performed by Aanesland. The first set of tests were performed fully submerged where the pipe was released with different angles just below the free surface. The second set of tests were performed with drops from above the free surface to investigate the effect of water entry on the final position of the pipe at the tank bottom. For the submerged tests, the initial angles between the submerged pipe axis and the free surface were $0°, 30°, 45°$ and $90°$. The drop tests were followed by numerical analyses based on slender body theory and a viscous correction with an artificial separation point x_{sep}. Aanesland's theoretical model showed a significant influence by varying x_{sep}/L between zero and 0.5. For analysis, $x_{sep}/L = 0.4$ was recommended. Aanesland applied the cross-flow principle for viscous drag resistance and indicated that the cross-flow Reynolds number varied between 1000 and 10000 with corresponding variation of drag coefficient between 1.0 and 1.2. He demonstrated that using a drag coefficient for cross-flow as either 1.0 or 1.2 did clearly influence the motion path.

3.1 Validation in the submerged phase

In the following, the theory in section 2 is solved numerically for case studies based on Aanesland's experiments. The numerical analyses are performed for submerged drops of scaled down "weight tubes" which are closed at both ends. The depth of the test basin is 5 m. The dimensions of the cylinders are presented in Table 3.

Table 3: Pipe characteristics according to Aanesland (1987)

Dimension	*Value*
Length	450 mm
Diameter	10 mm
Mass per meter	0.548 kg/m

Our analyses are benchmarked with Aanesland's submerged drop tests performed with initial angles of 30°, 45° and 60°. The analyses of the submerged drops have been performed with an upstream drag coefficient C_{DU} that is half the value of the steady state coefficient $C_{D\infty}$. As presented in section 2.5 and eq. (24), this means that we set $t' = \frac{s}{R} + 1.4$ in the expression for C_D. For $C_{D\infty} = 1.1$, this implies a base value at the upstream end equal to $C_{DU} = 0.55$. The lift coefficient associated with asymmetric vortex shedding is set to $C_{La} = 0.25$.

Figure 5, 6, and 7 show comparisons of the motions of the center of gravity of the pipe for drop angles 30°, 45° and 60°, respectively. The figures present the drop path of the 3D analyses using our model compared to the maximum and minimum envelopes of Aanesland's test. For the 60° drop angle, it was reported that the pipe touched the bottom of the tank at an angle tangential to the tank floor. This is similar to the response observed for the analysis using the base values for $C_{D\infty}$ and C_{DU}. For initial drop angles of 30° and 45°, it is observed that the drop trajectory has a falling leaf pattern that falls within the envelope of Aanesland's tests.

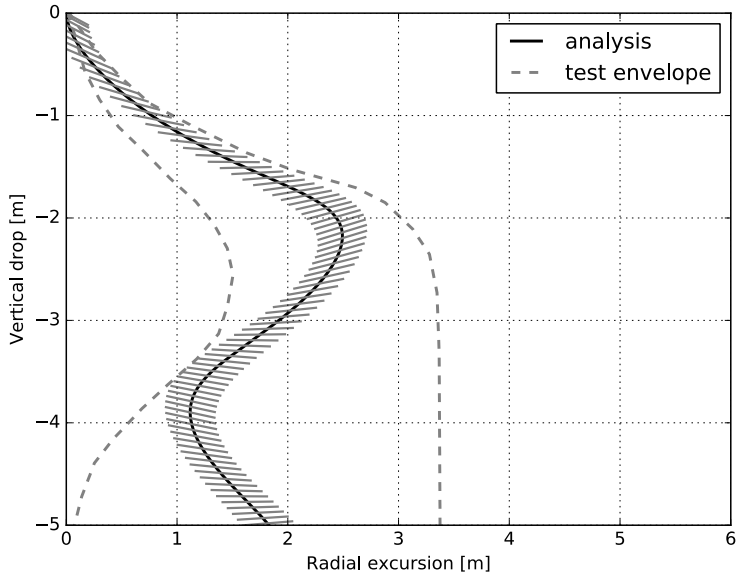

Figure 5: Drop trajectory for the 30°*submerged drop. Stapled lines illustrate the envelope from Aanesland's tests*

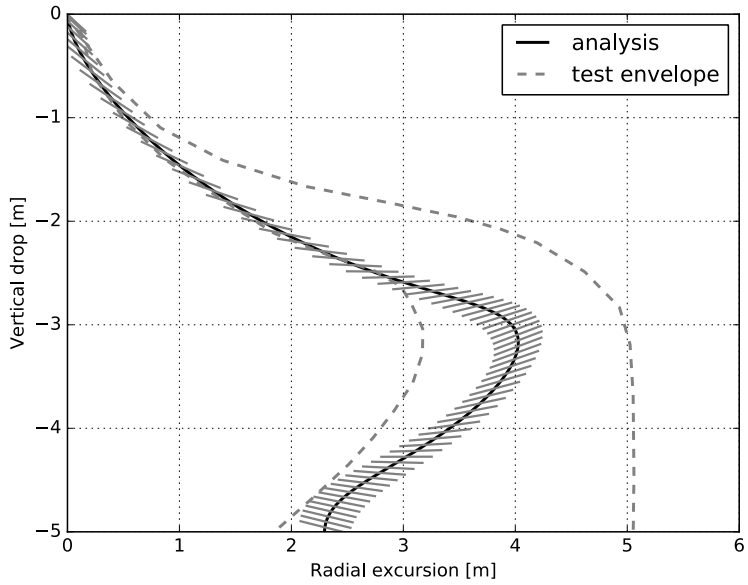

Figure 6: Drop trajectory for the 45° *submerged drop. Stapled lines illustrate the envelope from Aanesland's tests*

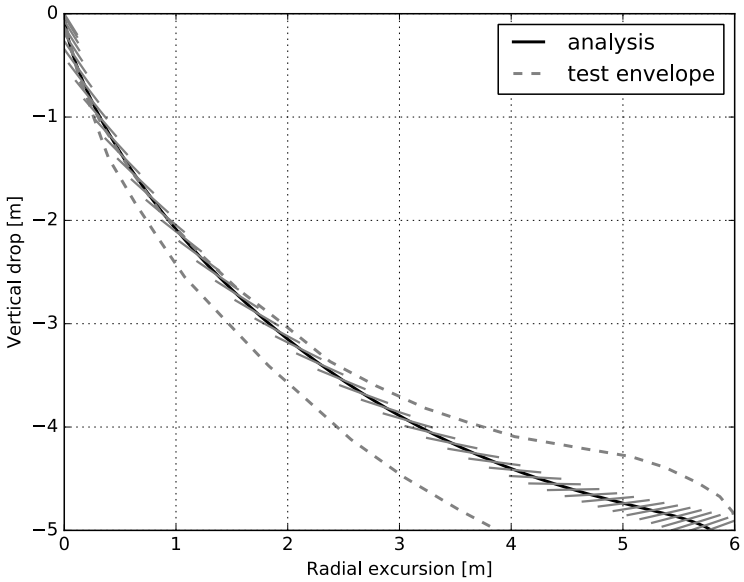

Figure 7 Drop trajectory for the 60° *submerged drop. Stapled lines illustrate the envelope from Aanesland's tests*

The velocity profile longitudinal and transverse to the pipe for the three drop angles are presented in Figure 8. It is observed that the transverse velocity at COG for drop angles 30° and 60° settles at around 0.9 m/s, followed by small oscillations as the falling leaf behavior develops. Peak forward velocity is developed between the release time and the point of maximum excursion. As observed, the maximum forward component varies between 2 m/s to 4 m/s, depending on initial drop angle. This corresponds to a Reynholds number above 10^6 for before the pipe reaches maximum excursion, which suggests turbulent boundary layer flow.

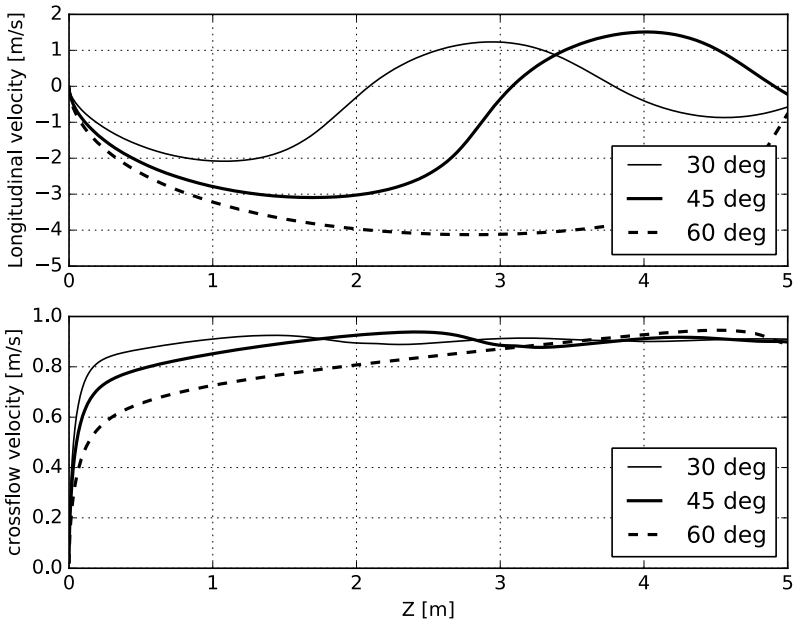

Figure 8: Velocity profiles for submerged drop cases with initial drop angles $30° - 60°$*. Longitudinal and cross-flow velocities at COG are plotted towards global vertical positions.*

It is interesting to compare the effects of drag model on the drop response of the pipe. In Figure 9, the trajectories of the dropped pipe using both *2D+t* theory and the cross-flow principle are compared. In the case of *2D+t* theory, the same base values for C_{DU} and $C_{D\infty}$ are applied with values 0.55 and 1.1, respectively. For the cross-flow principle, $C_{D\infty}$ is applied over the entire length of the pipe. From Figure 9 it is observed that the two drag models produce different responses for initial drop angles $30°$ and $60°$. In case of the $30°$.drop, the falling leaf behaviour starts earlier when applying 2D+t theory than when the cross-flow principle is applied, Figure 9 (a). At $60°$ drop angle the cross-flow principle and *2D+t* theory yields similar results in the 5 m depth range that is displayed. If the drop angle is further increased beyond $60°$, one can observe that the *2D+t* theory produces the falling leaf behaviour at larger depths than the cross-flow principle. This response is characteristic when comparing the two methods and can be reflected by considering the stationary problem without rotations. We then see that the combination of high forward speed and low transverse speed tends to pull the peak value of the drag coefficient distribution towards the pipe tail. The opposite scenario

pushes the drag coefficient distribution towards the nose of the pipe. This effect is visible when comparing our model towards equivalent analyses applying the cross-flow principle for small and steep drop angles.

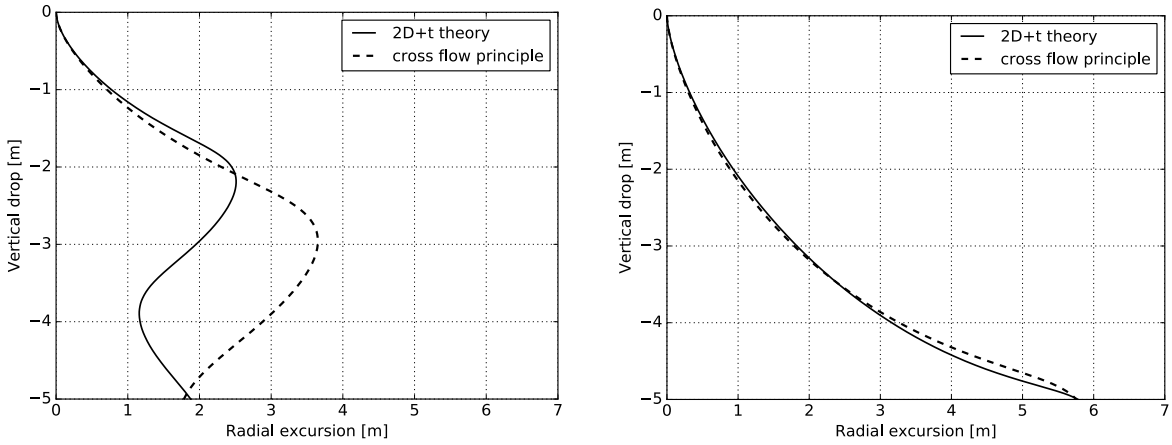

(a) (b)

Figure 9: Comparison of dropped object trajectories generated by 2D+t theory and the cross-flow principle. Trajectories for initial submerged drop angles (a) 30° *and (b)* 60° *are presented.*

3.2 Error analysis

In the following an error analysis of for the chosen parameters is performed. Error sources in our model for the submerged phase are:

- Added mass acceleration loads
- Viscous resistance
- Initial perturbations
- Upstream drag coefficient C_{DU} used in the *2D+t* theory
- Steady-state drag coefficient $C_{D\infty}$ used in the *2D+t* theory
- Lift coefficient amplitude C_{La} associated with asymmetric separation

The influence of varying added mass acceleration loads, and viscous resistance is small. The mass of the pipe is much higher than the added mass components. Reducing the added mass coefficients to 70% of the potential-flow value, to qualitatively mimic the influence of cross-flow separation, has

very little effect on the response of the pipe. The viscous resistance was calculated by assuming combined laminar and turbulent flow. Variations in the order of $\pm 10\%$ on the axial drag yield little influence in response for the tested cases (30° and 60° drops). The effect of the pipe's weight in water when the nose points upwards is a far more important resistance component.

The influence of the other error sources (transverse drag) are performed by selecting values $\pm 10\%$ of the base values and independently investigating the influence on time and excursion to locations *B* and *C*, as illustrated in Figure 1(a). Here *B* and *C* represents excursions at maximum and tank bottom, respectively. Similarly, the durations t_B and t_C represents the time to reach points *B* and *C*. Note that any hydrodynamic effect of proximity to the tank bottom or impact is not considered in the analyses. An error associated with reaching maximum excursion *a* was calculated as

$$\Delta_B = \sqrt{(\Delta_B^{CDU})^2 + (\Delta_B^{CD\infty})^2 + (\Delta_B^{CLa})^2} \tag{27}$$

where $2\Delta_B^{CDU}$ is the difference in excursion length to point B by varying the base value of C_{DU} ±10%, combined with the base values of $C_{D\infty}$ and C_{La}. The same is performed to estimate Δ_C, Δ_{tB}, Δ_{tC}. The results are presented in Table 4.

Table 4: Error estimation for a ±10% variation of base values for $C_{DU}, C_{D\infty}$ and C_{La}.

Drop angle	Δ_B	Δt_B	Δ_C	Δt_C
30°	0.29	0.11	0.19	0.21
45°	0.49	0.18	0.46	0.07
60°	0.52	0.53	0.47	0.65

From Table 4 we observe, with a few exceptions, an increase in error estimates with increasing drop angle. The same tendency is observed when plotting the pipe trajectories for the same $C_{D\infty}$ and C_{DU} variations, see Figure 10-12. A reason for the increased spread in excursion with steeper drop angles may be that steep drop angles create high forward speed before the pipe becomes instable and turns. Small variations in time at the onset of oscillation will then have a large effect on the spatial position

of the instability taking place. Further, by varying C_{DU} we displace the peak drag value presented in Figure 4 either towards the nose or the tail of the pipe. Increasing C_{DU}, means pulling the peak coefficient in Figure 4 towards the nose of the pipe, while decreasing C_{DU} has the opposite effect. This may explain that high values for C_{DU} forces the pipe to start its oscillatory behaviour earlier than by lower C_{DU} values. The effect is not as visible for the 60° drop angle, as this case does not fully contain the turning motion before reaching the tank bottom.

Variations in $C_{D\infty}$ have a significant effect on the drop trajectory of the pipe, especially for steep drop angles. The same effect was also witnessed by Aanesland (1987), and Xiang et al. (2017), who both varied the drag coefficient 1-1.2 for the same tests using the cross-flow principle.

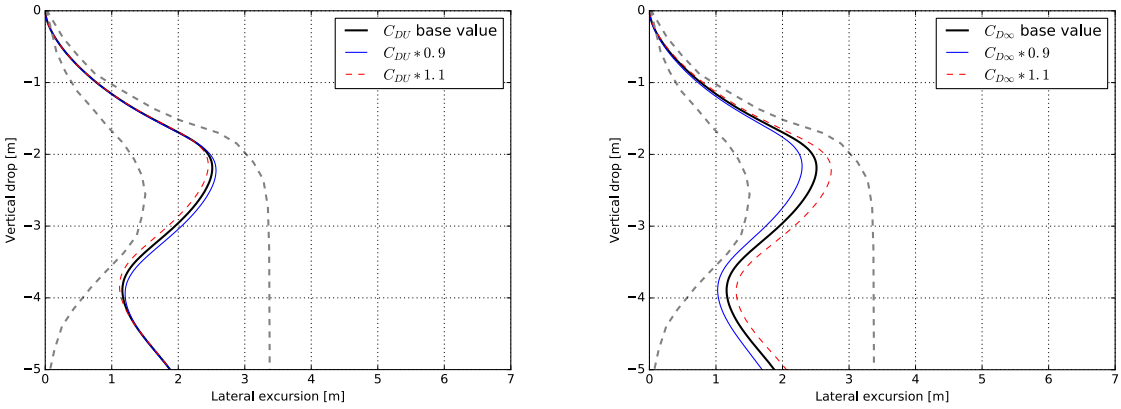

(a) (b)

Figure 10: Variation of 2D+t drag for 30° submerged drop, (a) drag at nose varied ±10% from its base value of 0.55; (b) $C_{D\infty}$ is varied by ±10% from its base value of 1.1

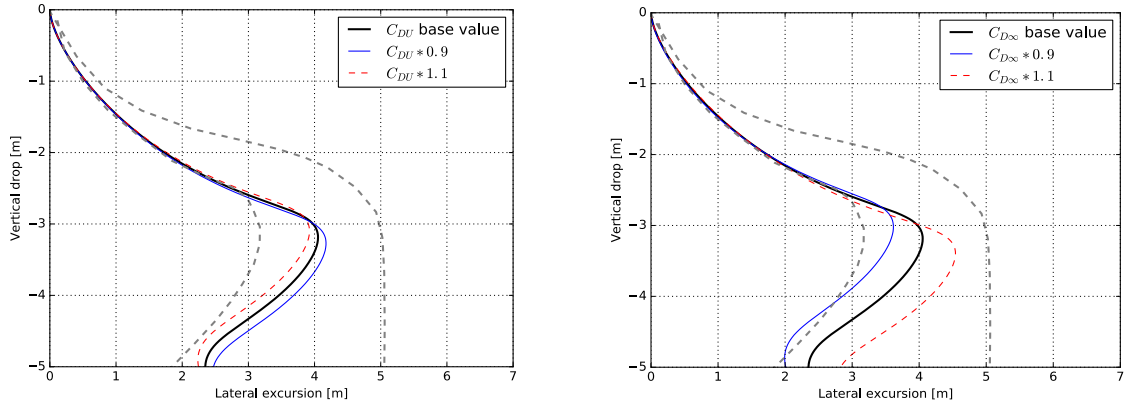

(a) (b)

Figure 11: Variation of 2D+t drag for 45° submerged drop, (a) drag at nose varied ±10% from its base value of 0.55; (b) $C_{D\infty}$ is varied by ±10% from its base value of 1.1

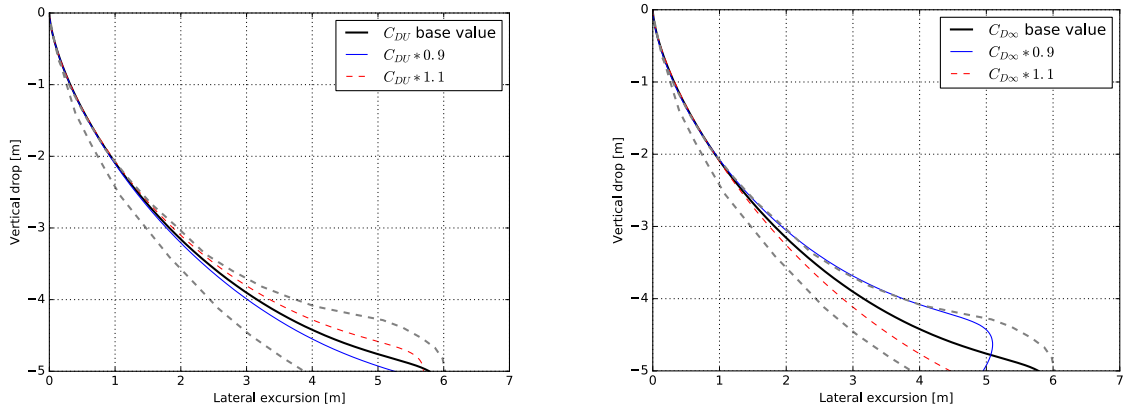

(a) (b)

Figure 12: Variation of 2D+t drag for 60° submerged drop, (a) drag at nose varied ±10% from its base value of 0.55; (b) $C_{D\infty}$ is varied by ±10% from its base value of 1.1

3.3 Evaluation of 3D effects

In our evaluation of three dimensional effects, we have proposed that the lateral motion from the dropped pipe may origin from non-symmetric vortex shedding along the length of the pipe. The effect is published by Sarpkaya (2010), and introduces a lateral pressure distribution on the pipe, which we estimate using eq. (25). In the analyses the lift coefficient amplitude, C_{La} , is set to 0.25. This is different from the methods applied by Xiang et al. (2017), who studied response of falling tubes subjected to the Magnus effect. In their analyses, they investigated the same drop cases as we do,

assuming the dropped pipes to have an initial roll velocity of 0.01 to 0.1 rad/s. It was claimed that this has a significant effect on out of planar motions. However, they applied a very high lift coefficient for their roll driven Magnus effect compared with experiments presented by Goldstein (1965) and Prandtl and Tietjens (1934). To exemplify, if we consider a rotating circular cylinder of radius R with a steady peripheral velocity $V_0 = pR$ in a constant cross-flow velocity U_0, the mean lift coefficient C_L is $2\pi V_0/U_0$ if adopting the approach of Xiang et al. (2017). However, Goldstein (1965) and Prandtl and Tietjens (1934) estimate by neglecting viscous effects that a maximum mean lift coefficient of 4π occurs at $V_0/U_0 = 4$. The latter is in fair agreement with the experimental results when end plates are used to minimize 3D flow effects. Xiang et al.'s (2017) formula is unrealistically conservative for the considered values of V_0/U_0 and gives, for instance, $C_L = 2\pi$ when $V_0/U_0 = 1$, while the experiments show $C_L = 1$. If we apply the same roll rate of 0.1 rad/s, as assumed by Xiang et al, we observe variations of V_0/U_0 in the order of 0.0005, which give very small values for C_L and negligible lateral forces. The Magnus effect has therefore not been considered further in this presentation.

The drop trajectory of the pipe is illustrated in Figure 13 for a range of initial drop angles varying between 0°-90°. All analyses are performed completely submerged and with the same input as presented for the base case analyses presented in section 3. For simplicity, the stochastic sign parameter K in eq. (25) is kept positive, i.e. K=1. The drop trajectory is shown in both the XZ and YZ planes. From the analyses, asymmetric flow separation as presented through eq. (25), provokes out of plane motions. Without this component, the pipe moves within the XZ plane.

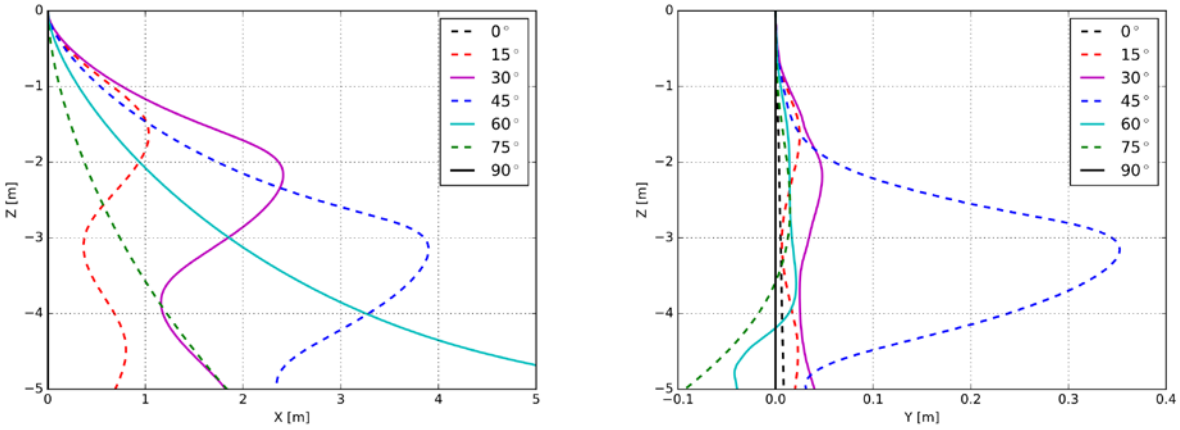

(b) (b)

Figure 13: XZ and YZ plane trajectories of submerged drops. Initial drop angles are varied 0° to 90°.

In Figure 14, the initial drop angle is varied between 0°-90° and the touch down coordinates at the tank bottom are registered. As seen from Figure 14, the out of plane excursion varies significantly with drop angle, which is strongest for drop angles between 60° and 70°. The sensitivity to drop angle is also observed from Figure 13(b) and is an effect of the sine formulation in eq. (25). This implies that out of plane forces and varies considerably with the variation of t'. The effect will be disturbed even further if the stochastic sign parameter K is activated.

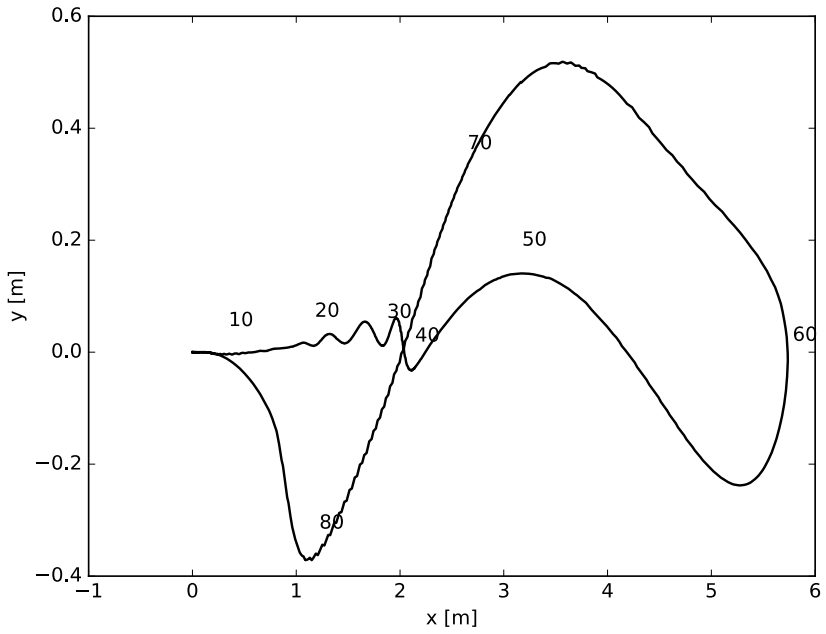

Figure 14: Drop excursion at 5 m depth (bottom of tank) using 2D+t theory and lateral lift effect. Initial drop angles towards the calm free surface is varied between 0° to 90°.

4 Cylinder dropped from air

4.1 Water entry

So far, we have only evaluated the dropped pipe behaviour for events that involve an initially submerged pipe. In addition to performing submerged drop tests, Aanesland (1987) also performed free fall tests from air using the same pipe dimensions. There, he applied the same drop angles and performed tests that involved a 1.48 m free fall, and water depths of 2.5 and 5 m. In the following, an attempt to describe the theory for the transient water impact phase and combine this with the description of the submerged phase presented in section 2. A numerical description of the drop behaviour is then finally compared with Aanesland's (1987) experiments.

When the dropped axisymmetric body is dropped from air, the body dynamics in air and during the water impact phase is essential in providing initial conditions for the fully submerged phase. When the angle between the body axis and the free surface is small, large water-impact loads associated with a

rapidly changing wetted surface, strong up-rise of water and air cavities occur. Mann et al. (2007) compared their approximate numerical method with field measurements by Richardson et al. (2001) of a horizontal cylindrical mine that was released 1.0 m above the water surface. The numerical and experimental vertical accelerations of the mine showed initially clear influence of air-cavity oscillations. The oscillation frequency can be explained by making an analogy to the natural frequency of a mass-spring system where the spring effect is due to compressibility of air and the mass is a generalized added mass caused by the cavity-induced pressure oscillations in the water Faltinsen (2005). Bodily et al. (2004) studied experimentally air cavity formation during vertical and nearly vertical water entry of slender axisymmetric bodies. Since the air-cavity oscillations die out on the time scale of a fully submerged simulation, the effect will be neglected. The fact that ricochet motion can occur for nearly horizontal water entry is not studied.

We assume planar motions in the air and water-impact phases. We will neglect aerodynamic loads and assume the body falls in air with a constant angle. The vertical impact velocity is then $\sqrt{2gh}$ where h is the drop height above the water surface. The effects of water waves and platform motions will not be considered. The described scenario during water entry (impact) is illustrated in Figure 15. A strip theory approach is followed and only the transverse hydrodynamic loads are considered. Campbell and Weinberg's (1980) experimental slamming coefficients and Faltinsen's (1990) description for water entry of a circular cylinder are used in the analysis. Large slamming forces are associated with large changes of the wetted area over a short time. The transverse slamming force per unit length is expressed as

$$f_z^{\text{slamming}} = -\frac{1}{2}\rho C_S D(w - xq)^2, C_S = \frac{5.15}{1 + \frac{19h}{D}} + 0.55\frac{h}{D}, \frac{h}{D} < 1 \quad (28)$$

Here, D is the cross-sectional external diameter. The submergence h of the cross-section relative to calm water level is defined in Figure 15.

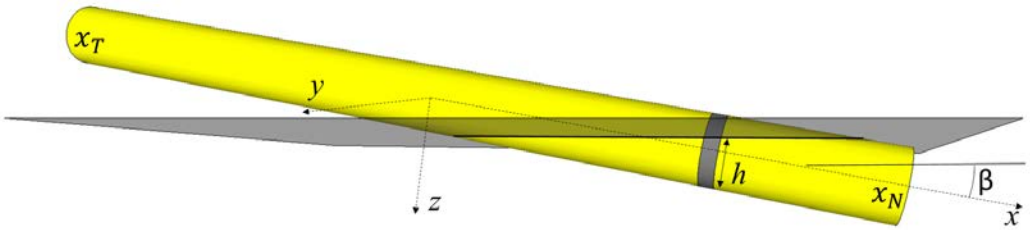

Figure 15: Water entry phase with partially wetted length.

Campbell and Weynberg (1980) demonstrated the validity of the formula for $|\beta| < 8°$ (see Figure 15 for a definition of β). We propose to use the formula for any β. When $h/D > 1$ in the slamming phase, C_s is proposed set constant for $h/D = 1$. Figure 16 compares for $\beta = 0$ the formula by Campbell and Weynberg (1980) with other experimental data and with numerical calculations based on potential flow with exact free-surface conditions as well as the approximate generalized Wagner model Chezhian (2003). Since the effect of viscosity can be considered negligible, the exact numerical result is a relevant comparison for the empirical method by Campbell and Weynberg (1980). Relevant error sources are three-dimensional flow and deceleration of the dropped object. The results in Figure 16 can be considered as a basis for prediction of predicted paths of a pipe dropped from air into water.

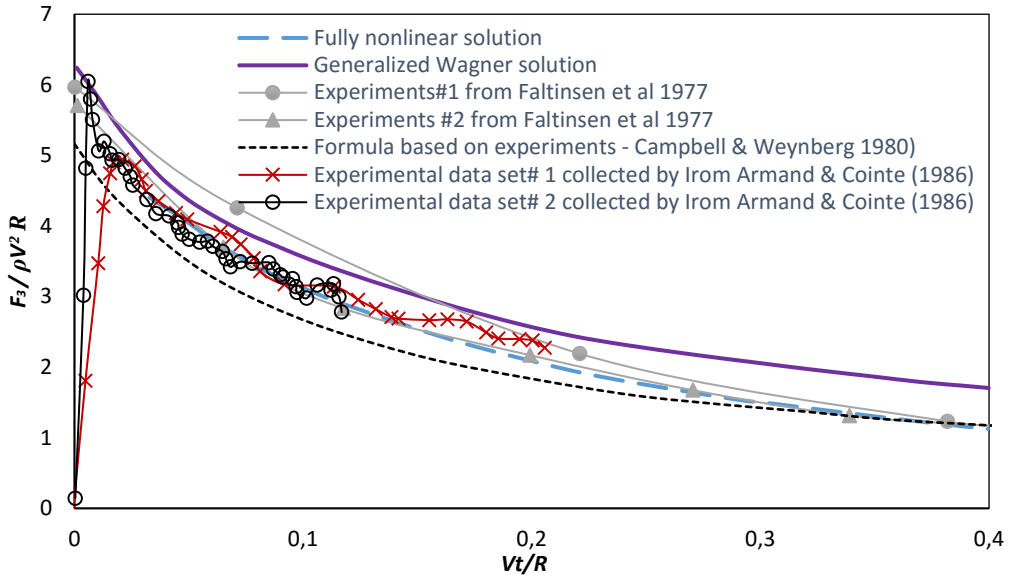

Figure 16: Slamming coefficient $C_S = F_3/\rho V^2 R$ for the water entry of a circular cylinder versus non-dimensional time Vt/R, using a fully nonlinear method, generalized Wagner method and published experimental results Chezhian (2005). The results are provided by Rong Zhao (unpublished, 2001)

In addition, added mass loads must be added by accounting for that a cavity is formed above the cross-section when $h > 0.5D$. The added mass loads per unit length in the *z*-direction is approximated as

$$f_z^{\text{added mass}} = -a_{33}(\dot{w} - x\dot{q}) \tag{29}$$

When $h \leq 0.5D$, the 2D heave added mass a_{33} with high-frequency free-surface condition for a partially submerged circular cylinder of radius *R* and draft *h* based on Lockwood Taylor (1930) is used, i.e.

$$\frac{a_{33}}{\rho\pi R^2} = \frac{\pi^2}{3}\frac{(1-\cos\theta)}{(2\pi-\theta)^2} + \frac{(1-\cos\theta)}{6} + \frac{\sin\theta - \theta}{2\pi}, \quad \text{where } \theta = 2\arccos(1-h/R) \tag{30}$$

When $h > 0.5D$ and $a_{33} = 0.125\rho\pi D^2$.

The collapse time of the cavity depends on the Froude number with cross-flow impact velocity as characteristic length and the diameter as characteristic length (Faltinsen et al., 1977). We may

pragmatically assume that the slamming phase is over when $h/D = 2$. The sensitivity to this assumption is a matter of investigations. When high slamming loads occur, we can neglect hydrostatic and viscous loads in solving the equations of motions.

4.2 Validation of drops from above the free surface

The air-water response of dropped cylinders has been documented trough experiments recorded at high speed by Ueda et al (2011) for L/D ratios equal to 25. The cylinders had a diameter of 12 mm, length of 300 mm and density of 1258 kg/m^3. Ueda monitored the response of both hydrophobic and hydrophilic surfaces. Only the response of the hydrophilic cylinder is investigated herein.

Ueda et al. (2011) dropped cylinders from a height of 200 mm, with a 36° drop angle to the free surface. From the test on hydrophilic material, local air cavities formed at both ends of the cylinder when passing through the water surface. The cavity at the cylinder nose stretched a couple of diameters behind the upstream end and collapsed off the cylinder at about 5-6 diameters depth. The cavity at the tail of the cylinder showed similar characteristics as the upstream end.

The drop response of the test by Ueda et al. is reproduced numerically using slamming and added mass theory as presented in section 4.1. As observed from high speed photos presented by Ueda et al, the cylinder rotates at water impact. When fully submerged, the cylinder had an approximate angle of 15° to the waterline. This took place about 0.085 s after first water entry, see fig 2 (g) in Ueda et al (2011). For comparison, our numerical model rotates to an angle of about 14° to the waterline when the tail is fully submerged. This takes place 0.078 s after entering the water, which implies an 8% difference in duration of the slamming phase. After this point, the pipe is considered fully submerged. The numerical response is illustrated in Figure 17. It is realized that although our one-point validation of our slamming model shows agreement with Ueda's experiment, it is a lightweight validation of the model. However, in lack of other data, the model will be applied for numerical reproduction of the drop tests from above the free surface by Aanesland (1987).

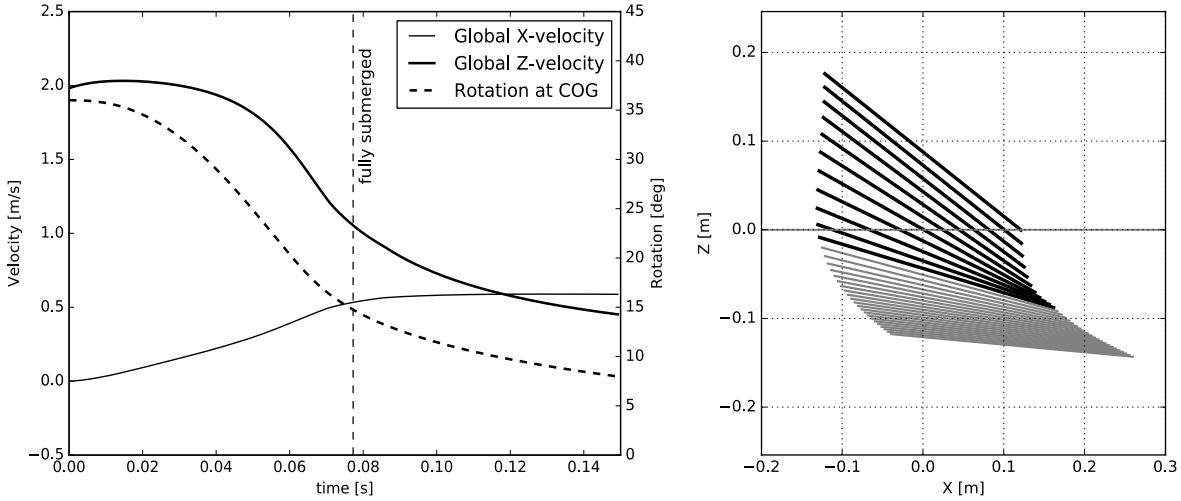

(a) (b)

Figure 17: Water entry response from simulation of a hydrophilic cylinder (L=300mm, D=12mm, ρ=1258 kg/m^3) dropped from a height of 200 mm at and angle to the free surface of 36°. *Figure (a) shows the global velocities in X and Z directions of the COG (y-axis on left side) and angular variation in degrees (y-axis on right side). Figure (b) shows the spatial response as the cylinder enters water.*

4.3 Analysis of Aanesland's above free surface drop experiments

In the following, we describe four sets of drop tests from above the free surface presented by Aanesland (1987), and Aanesland and Huse (1986). The drop tests were carried out from a drop height of 1.48 m above the free surface for drop angles 30° and 60°. For each drop angle, two depth variations were tested; 2.5 m and 5 m. Within each drop scenario, 8-14 drop tests were performed. The final impact locations at the tank bottom are presented in figure 18. As observed from the digitized plots, the 30° case indicates that the final position of the dropped pipes cluster together into two locations, which is especially visible for the 5 m depth case. Whether this is due to oscillatory behavior or drops simply being performed at 30° or −30° degrees are unclear. It is, however, interesting to observe that the clusters of pipes are positioned at about 1 m radially from the drop center and that the pipes have a heading in the plane it was dropped.

The 60° drop tests introduce a fan shaped scatter. For the 5 m depth cases, maximum excursion is about 5 m, while the minimum excursion is about 2 m. For the 2.5 m depth scenario, Figure 18 (b) the pipes are more spatially focused. The reason for this pattern, may be that at 2.5 m depth, the pipe has not reached the maximum excursion point, while at 5 m depth, the pipe has reached the falling leaf behavior. See for instance Figure 19 (b).

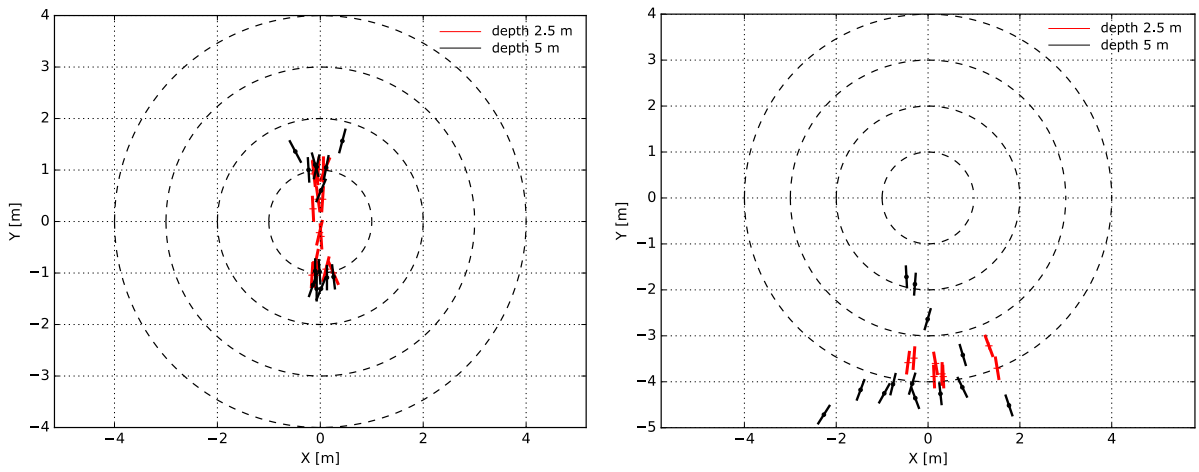

(a) (b)

Figure 18: Birds eye view of final positions of pipes dropped from air to water. Figure shows (a) 30° degree drop angle, and (b) 60° drop angle. Water depth is 2.5 m (red), and 5m (black). Drop height is 1.48 m. Test data extracted from, Aanesland & Huse (1986)

The four drop scenarios presented in Figure 18 have been reproduced by numerical analysis using theory outlined in section 2 and 4.1. Our analyses are split in two phases, water entry and submerged phases, respectively. As seen from Aanesland's experiments, we see for some cases a noticeable scatter occurs in the lateral direction. We see from analyses that we as well can create an out of plane scatter, but not to the same extent as in the tests. To do so we must vary initial conditions, or parameters such as $C_{DU}, C_{D\infty}$ and C_{La}, all which we have limited information about. We thus restrict ourselves only to consider the radial trajectory using the input from the slamming phase and continue the submerged phase with the same base values as for the submerged drops. The results of the analyses are presented in Figure 19 and compared with histograms showing the hit-locations of the tests. The bin interval of the histogram is about 10 cm. For the 30° drop cases, the hit points are in dense and

clustered zones. By comparing the numerical analyses for the 30° drop angle, Figure 19 (a), it is observed that the trajectory of the simulation aligns with the registered hit points from experiments. The same is observed for the series of drops with initial angle of 60° degrees, which predicts the excursion at both 2.5 and 5 m reasonably well. It is worth mentioning here, that we only analyze the trajectory of the pipe and disregard any effects or contact with ground. This means that we also disregard possible sliding effects after the pipe touches ground, as may be the case for the 60° drop at 2.5 water depth. Finally, as observed in section 4.2, the water entry phase introduces initial conditions for the submerged phase (pitch rotation, and velocity components) which alters the trajectory for the submerged phase. If we, for instance, compare the trajectory of the 60° drop angle from Figure 19 with the equivalent submerged drop presented in Figure 12, we see that the drop from above the free surface reaches the maximum excursion at shallower depth than the submerged drop. This is important and verifies that initial conditions passed on from the water entry phase to the submerged phase needs to be accounted for to predict the touch down position on the seabed.

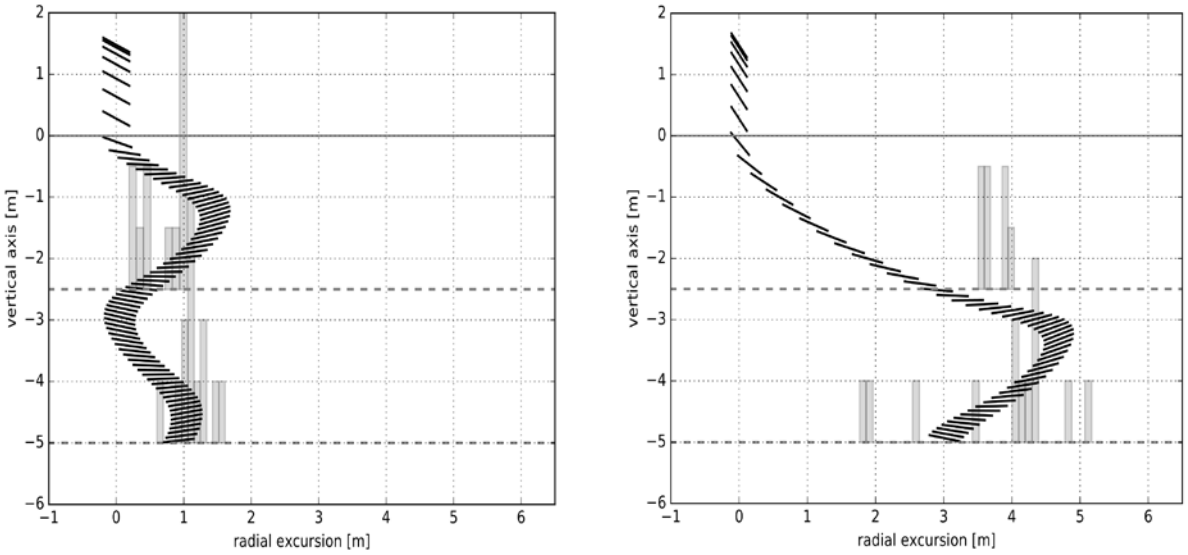

(a) (b)

Figure 19: Comparison between numerical analyses and measured hit locations for initial drop angles; (a) 30° *and (b)* 60°*. Two water depths are recorded: 2.5 m and 5 m. Drop height above water is 1.48 m.*

5 Conclusions

Cylinder shaped objects lifted from offshore support vessels to offshore rigs comprise a significant part of the dropped object potential for subsea structures and pipelines. Existing methods for characterizing the risk level for failure of production systems due to dropped object impacts are very coarse and simplified. The presented 3D theory provides a methodology that can provide a rational and deterministic description of how the pipe travels through water when dropped to sea. This is important as it provides better information of the radial reach of dropped objects and their kinetic energy at impact. As the presented method is simplified, it is also computationally efficient. It implies that a large set of analyses can be performed to establish a statistical representation of hit location and impact energy. In turn this may be applied in risk based dropped object analyses. The latter discussion is, however, beyond the scope of this paper. Our focus is in the deterministic response of the falling pipe.

In the investigation of the dropped pipe response, our main contribution is the introduction of *2D+t* theory and application of Sarpkaya's work on transverse drag. This is important as forward speed will affect the development of vortices downstream the pipe nose, and hence affect the drag force and moment on the pipe. Application of the model shows in general a good correlation with tests performed by Aanesland (1987).

Our analyses using *2D+t* theory introduces some modifications to Sarpkaya's representation of the evolution of the impulsive flow and hence the representation of the drag coefficients. As the nose of the pipe is blunt, we assume separation at the nose section and introduce an initial drag, C_{DU}, which is half its steady value $C_{D\infty}$. Comparison with experiments by Reif and Powell (1917), suggest that this is reasonable, and so do our analyses of the dropped pipe. Variation of the above coefficients indicate that the system is sensitive to changes, and further studies on other pipe geometries should therefore be undertaken to further verify C_{DU} and $C_{D\infty}$.

The effect of non-planar motion is investigated. To introduce out of plane motions, a lateral driving force is required. This is obtained by introducing the *2D+t* theory and the effect of non-symmetric vortex shedding along the cylinder as it travels through water. This generates lateral lift forces and yaw moments, which in turn twists the trajectory of the pipe. Our approximation of lateral forces is based on lateral lift coefficients derived from tests, Sarpkaya (2010). This is presented in eq (25) using a lift coefficient C_{La} of 0.25. We emphasize that direct comparison towards test have not been performed. Further studies should therefore be performed to verify the formulation of eq (25) and the magnitude of C_{La}. Lift forces generated by the Magnus effect is also introduced using roll rates in the order of 0.1 rad/s, as investigated by Xiang et al. (2017). However, with basis in experiments performed by Goldstein (1965) and Prandtl and Tietjens (1934), analyses indicated that the Magnus effect was negligible for the magnitude of the considered roll velocity. It is thus concluded that out of plane motion is a result of other effects, where asymmetric vortex separation is considered as a likely candidate.

In addition to the submerged phase, the water entry phase is described. This is performed by introducing the slamming load and varying added mass. Both are distributed over the wetted length of the pipe as it enters the water. An important effect of this is that the slamming phase introduces a transient change in pitch angle, and pitch rate, which has a significant effect on the following submerged phase. Comparison between tests and analyses shows reasonable correlation between hit locations at the seabed when investigating the radial excursion. The tests further show a large spread in lateral and radial excursion. The reason for this spread is not attempted explained herein. We only investigate the correlation between analyses and how they correlate with the distribution of hit location from the tests.

For the future, the model should be further verified towards experiments. This implies that more tests need to be performed in order to form a basis for an extended verification. New experiments should address variations in L/D ratio, weight and position of the COG. It is also recommended that more work is carried out to further study 3D effects at the pipe nose and its effect on the flow separation. This can provide a better foundation for quantifying the development of cross flow drag and lateral lift forces on the falling pipe. This may further be important when considering variations in geometry such as L/D ratio or effects from potential end flanges.

6 References

Aanesland V. and Huse E., (1986), *Experimental and Numerical Investigation of Accidental Drops of Drilling Tubes*, MARINTEK report 86-0139-520075

Aanesland, V. (1987). Numerical and experimental investigation of accidentally falling drilling pipes. OTC 5497, *19th Annual Offshore Technology Conference (OTC),* Houston, Texas.

Bodily, K. G., Carlson, S. J., Truscott, T. T., (2004). The water entry of slender axisymmetric bodies, *Physics of Fluids*, 22.

Campbell, I. M. C., Weinberg, P. A. (1980). *Measurements of parameters affecting slamming*. Final report, Rep. No. Technology Reports Center, No. OT-R-8042, Southampton University; Wolfson Unit for Marine Technology.

Chezhian, M., (2003). *Three-dimensional Analysis of Slamming*. PhD thesis 2003:85, Dept. of Marine Technology, Norwegian University of Science and Technology. IMT-2003-3.

Chu, P., Gilles, A., Fan, C. (2005). Experiment of falling cylinder through the water column. *Experimental Thermal and Fluid Science*, 29, 55-568.

DNVGL(2017a), *Recommended Practice, DNVGL-RP-C204, Design against Accidental Loads*, August 2017

DNVGL (2017b), *Recommended Practice, DNVGL-RP-C107, Risk Assessment of Pipeline Protection*, May 2017

Durante, D., Broglia, R., Muscari, R., Di Mascio, A. (2010). Numerical simulations of a turning circle manouvre for a fully appended hull. *Proc. 28th ONR Symposium on Naval Hydrodynamics*, Pasadena, USA. 12-17 Sept.

Ersdal, S, Faltinsen, O.M. (2006). Normal forces on cylinders in near-axial flow, *J. Fluids and Structures.*V 22, Issue 8, pp 1057-1077.

Faltinsen, O. M., Kjærland, O., Nøttveit, A., Vinje, T. (1977). Water impact loads and dynamic response of horizontal cylinders in offshore structures, *9th Annual Offshore Technology Conference (OTC)*, Houston, Texas.

Faltinsen, O.M., Kjærland, O., Liapis, N., Walderhaug, H., (1979), Hydrodynamic analysis of tankers at single-point-mooring systems, *BOSS '79*, London.

Faltinsen, O. M. (1990) *Sea Loads on Ships and Offshore Structures*, Cambridge University Press.

Faltinsen, O. M. (2005). *Hydrodynamics of High-Speed Marine Vehicles.* Cambridge University Press.

Goldstein, S. (1965). *Modern Developments in Fluid Dynamics.* Dover Publications.

Hoerner, S. F. (1958). *Fluid Dynamic Drag.*

Kochin, N. E., Kibel, I. A., Roze, N. V. (1964). *Theoretical Hydromechanics.* Interscience Publishers.

Lamont, P. J., Hunt, B. L. (1976). Pressure and force distributions on a sharp-nosed circular cylinder at large angles of inclination to a uniform subsonic stream. *J. Fluid Mech*., 76, 519-59.

Mann, J., Liu, Y., Kim, Y., Yue, D.K.P. (2007). Deterministic and stochastic predictions of motion dynamics of cylindrical mines falling through water, *IEEE Journal of Oceanic Engineering*, 32, 1.

Prandtl, L., Tietjens, O. G. (1934). *Applied Hydro- and Aeromechanics.* Dover Publications

Richardson, M., Valent, P., Briggs, K., Bradley, J., Griffin, S. (2001). NRL mine burial experiments, *Proc. 2nd Austr. -Amer. Joint Conf. Technol. Mine Countermeas.*, Sydney, Australia, 1-23.

Reif, E. F., Powell, C. H., (1917). Tests of smooth and stranded wires inclined to the wind direction, and a comparison of results on stranded wires in air and water. *ARC Reports and Memoranda.*

Sarpkaya, T., (1966). Separated flow about lifting bodies and impulsive flow about cylinders. *AIAA J.* 17, 1193-1200.

Sarpkaya, T., (2010), *Wave Forces on Offshore Structures*, Cambridge University Press. ISBN-13: 9780521896252

Schlichting, H. (1979), *Boundary Layer Theory*, McGraw-Hill, ISBN 0-07-055334-3

Taylor, J. L., (1930). Some hydrodynamic inertia coefficients, *Phil. Mag.* 9(7), 161-183.

Ueda, Y., Uemura, T., Iguchi, M. (2011), Entry of inclined hydrophobic and hydrophilic circular cylinders into water, *Journal of Visualization*, Vol 14-1, 7-9.

Valent, P. J., Holland, T. K. (2001). *Quick look report: Model mine hydrodynamic tests.* Naval Surface Warfare Center (NSWC), Carderock Division, West Bethesda, MD, NRL Internal Memorandum

Werle, H. (1979). Vortices on slender bodies at high angles of attack. *L'Aeronautique et l'Astronautique*, 79, 3-22,

White, F. M. (1972). An analysis of axisymmetric turbulent flow past a long cylinder, *J. Basic Eng. ASME*, Vol. 94, pp. 200-208.

Xiang, G., Birk, L., Yu, X., Lu, H. (2017). Numerical study on the trajectory of dropped cylindrical objects, *Ocean Engineering*, 130, 1-9.

Zdravkovich, M. M. (2003). *Flow around Circular Cylinders. Vol2: Applications*. Oxford Science Publications.